IOPscience iopscience.iop.org

Home Search Collections Journals About Contact us My IOPscience

Six-field two-fluid simulations of peeling–ballooning modes using BOUT++

This article has been downloaded from IOPscience. Please scroll down to see the full text article.

2013 Nucl. Fusion 53 073009

(http://iopscience.iop.org/0029-5515/53/7/073009)

View the table of contents for this issue, or go to the journal homepage for more

Download details:
IP Address: 128.15.244.100
The article was downloaded on 18/06/2013 at 05:08

Please note that terms and conditions apply.

IOP Publishing and International Atomic Energy Agency | Nuclear Fusion

Nucl. Fusion **53** (2013) 073009 (12pp) doi:10.1088/0029-5515/53/7/073009

Six-field two-fluid simulations of peeling–ballooning modes using BOUT++

T.Y. Xia[1,2], **X.Q. Xu**[2] **and P.W. Xi**[2,3]

[1] Institute of Plasma Physics, Chinese Academy of Sciences, Hefei,
People's Republic of China
[2] Lawrence Livermore National Laboratory, Livermore, CA 94550, USA
[3] FSC, School of Physics, Peking University, Beijing, People's Republic of China

E-mail: xiaty@ipp.ac.cn

Received 31 December 2012, accepted for publication 3 May 2013
Published 24 May 2013
Online at stacks.iop.org/NF/53/073009

Abstract

The simulations on edge-localized modes (ELMs) with six-field peeling–ballooning (P–B) modes using the BOUT++ code are reported in this paper. This six-field model based on the full Braginskii equations are developed to simulate self-consistent turbulence and transport between ELMs. Through the comparison with the previous three-field two-fluid model, P–B instability, ion diamagnetic effects, resistivity and hyper-resistivity are found to be the dominant physics during ELMs. The additional physics, such as ion acoustic waves, thermal conductivities, Hall effects, toroidal compressibility and electron–ion friction, are less important in this process. Through the simulations within different equilibrium temperature profiles but with the same pressure and current, the particle loss of ions contributes the least to the total ELM size. The ELM size will be smaller for low-density cases. The study of convective particle and heat flux indicates that the peak of radial particle flux is obviously related to the ELM filaments burst events. The analysis of radial transport coefficients indicates that the ELM size is mainly determined by the energy loss at the crash phase. The typical values for transport coefficients in the saturation phase after ELM crashes are $D_r \sim 200\,\mathrm{m}^2\,\mathrm{s}^{-1}$, $\chi_{ir} \sim \chi_{er} \sim 40\,\mathrm{m}^2\,\mathrm{s}^{-1}$. The turbulent zonal flow, which is mainly driven by the Reynolds stress and suppressed by ion diamagnetic terms, regulates the turbulence from the ELM crash phase to the quasi-steady state for large ELM cases.

(Some figures may appear in colour only in the online journal)

1. Introduction

To assess the performance requirements of future tokamaks, such as ITER, one must study [1] discharges in the high edge particle and energy confinement regime known as H-mode [2]. In ELMy H-mode, edge-localized modes (ELMs) are triggered by ideal magneto-hydrodynamic (MHD) instabilities. The onset of the type I ELM is successfully explained by ideal peeling–ballooning (P–B) theory in the pedestal [3], whereby the steep pressure gradients drive ballooning modes and bootstrap current generates peeling modes. The understanding of the linear P–B mode has been well developed by study with numerical codes such as ELITE [4, 5] and GATO [6]. However, linear stability analysis alone is not enough to describe the whole picture of ELM physics. The nonlinear phase is also very important for ELM studies. Some 3D codes have been developed for the nonlinear simulation of ELMs, including NIMROD [7, 8], BOUT [9, 10], JOREK [11], etc.

The BOUT++ code has successfully simulated the nonlinear crash phase of ELMs [12–15]. In the previous work, anomalous electron viscosity or hyper-resistivity is included in Ohm's law. This method resolves the computational difficulty of the fine resolution requirement for ideal MHD instabilities with high Lundquist number. The four-field two-fluid model has been developed as the extension of the previous three-field P–B model with the addition of perturbed parallel velocity. For linear runs we find this parallel velocity perturbation could stabilize the P–B modes and decrease the linear growth rate and ELM size [16]. The $\boldsymbol{E} \times \boldsymbol{B}$ shear flow plays a dual role on P–B modes [17]. On the one hand, the flow shear can stabilize high-n P–B modes and twist the mode in the poloidal direction, constraining the mode's radial extent and reducing the size of the corresponding ELM. On the other hand, the shear flow also introduces the Kelvin–Helmholtz mode, which can destabilize the P–B modes. The theoretical and simulation results of a gyro-Landau-fluid (GLF) extension of the BOUT++ code are summarized in [18], which contributes to increasing the physics understanding of ELMs.

In this paper we develop the nonlinear simulations of the six-field P–B model with BOUT++ code based on the reduced MHD model [20]. This paper is organized in the following way. The physics models and the formula used in our simulations are in section 2. Section 3 shows the linear and nonlinear simulations results. The comparisons among

© 2013 IAEA, Vienna Printed in the UK & the USA

the six-field, five-field and three-field models are shown at the beginning of this section. Then the effects of normalized density on ELM size, density flux and heat flux are discussed. The calculations of transport coefficients for radial particle and heat fluxes follow. At the end of this section, the turbulent zonal flow is discussed. The last section is the summary.

2. Physics models and equations

In this paper, we simulate the nonlinear collapse process of edge pedestal plasmas using a six-field two-fluid model in tokamak configuration. Starting from the Braginskii equations, within the flute reduction, our six-field model is constituted of six evolving equations based on [20, 19], which are written in drift ordering as

$$\begin{aligned}\frac{\partial}{\partial t}\varpi = & -\frac{1}{B_0}\boldsymbol{b}\times\boldsymbol{\nabla}_\perp\Phi\cdot\boldsymbol{\nabla}\varpi + B_0^2\nabla_\parallel\left(\frac{J_\parallel}{B_0}\right)\\ & + 2\boldsymbol{b}\times\boldsymbol{\kappa}\cdot\boldsymbol{\nabla}P_\mathrm{i} - \frac{1}{2\Omega_\mathrm{i}}\left[\frac{1}{B_0}\boldsymbol{b}\times\boldsymbol{\nabla}P_\mathrm{i}\cdot\boldsymbol{\nabla}\left(\nabla_\perp^2\Phi\right)\right.\\ & \left. - Z_\mathrm{i}eB_0\boldsymbol{b}\times\boldsymbol{\nabla}n_\mathrm{i}\cdot\boldsymbol{\nabla}\left(\frac{\nabla_\perp\Phi}{B_0}\right)^2\right]\\ & + \frac{1}{2\Omega_\mathrm{i}}\left[\frac{1}{B_0}\boldsymbol{b}\times\boldsymbol{\nabla}\Phi\cdot\boldsymbol{\nabla}\left(\nabla_\perp^2 P_\mathrm{i}\right)\right.\\ & \left. - \nabla_\perp^2\left(\frac{1}{B_0}\boldsymbol{b}\times\boldsymbol{\nabla}\Phi\cdot\boldsymbol{\nabla}P_\mathrm{i}\right)\right] + \mu_{\parallel\mathrm{i}}\nabla_{\parallel 0}^2\varpi,\end{aligned} \tag{1}$$

$$\begin{aligned}\frac{\partial}{\partial t}n_\mathrm{i} = & -\frac{1}{B_0}\boldsymbol{b}\times\boldsymbol{\nabla}_\perp\Phi\cdot\nabla n_\mathrm{i} - \frac{2n_\mathrm{i}}{B_0}\boldsymbol{b}\times\boldsymbol{\kappa}\cdot\boldsymbol{\nabla}\Phi\\ & -\frac{2}{Z_\mathrm{i}eB_0}\boldsymbol{b}\times\boldsymbol{\kappa}\cdot\boldsymbol{\nabla}P_\mathrm{i} - n_\mathrm{i}B_0\nabla_\parallel\left(\frac{V_{\parallel\mathrm{i}}}{B_0}\right),\end{aligned} \tag{2}$$

$$\frac{\partial}{\partial t}V_{\parallel\mathrm{i}} = -\frac{1}{B_0}\boldsymbol{b}\times\boldsymbol{\nabla}_\perp\Phi\cdot\boldsymbol{\nabla}V_{\parallel\mathrm{i}} - \frac{1}{m_\mathrm{i}n_\mathrm{i0}}\boldsymbol{b}\cdot\boldsymbol{\nabla}P, \tag{3}$$

$$\begin{aligned}\frac{\partial}{\partial t}A_\parallel = & -\nabla_\parallel\phi + \frac{\eta}{\mu_0}\nabla_\perp^2 A_\parallel + \frac{1}{en_\mathrm{e0}B_0}\nabla_\parallel P_\mathrm{e} + \frac{0.71k_\mathrm{B}}{eB_0}\nabla_\parallel T_\mathrm{e}\\ & - \frac{\eta_\mathrm{H}}{\mu_0}\nabla_\perp^4 A_\parallel,\end{aligned} \tag{4}$$

$$\begin{aligned}\frac{\partial}{\partial t}T_\mathrm{i} = & -\frac{1}{B_0}\boldsymbol{b}\times\boldsymbol{\nabla}_\perp\Phi\cdot\boldsymbol{\nabla}T_\mathrm{i}\\ & -\frac{2}{3}T_\mathrm{i}\left[\left(\frac{2}{B_0}\boldsymbol{b}\times\boldsymbol{\kappa}\right)\cdot\left(\boldsymbol{\nabla}\Phi + \frac{1}{Z_\mathrm{i}en_\mathrm{i0}}\boldsymbol{\nabla}P_\mathrm{i} + \frac{5}{2}\frac{k_\mathrm{B}}{Z_\mathrm{i}e}\boldsymbol{\nabla}T_\mathrm{i}\right)\right.\\ & \left. + B_0\nabla_\parallel\left(\frac{V_{\parallel\mathrm{i}}}{B_0}\right)\right] + \frac{2}{3n_\mathrm{i0}k_\mathrm{B}}\nabla_{\parallel 0}\left(\kappa_{\parallel\mathrm{i}}\nabla_{\parallel 0}T_\mathrm{i}\right)\\ & + \frac{2}{3n_\mathrm{i0}k_\mathrm{B}}\boldsymbol{\nabla}_\perp\cdot\left(\kappa_{\perp\mathrm{i}}\boldsymbol{\nabla}_\perp T_\mathrm{i}\right) + \frac{2m_\mathrm{e}}{m_\mathrm{i}}\frac{Z_\mathrm{i}}{\tau_\mathrm{e}}\left(T_\mathrm{e} - T_\mathrm{i}\right),\end{aligned} \tag{5}$$

$$\begin{aligned}\frac{\partial}{\partial t}T_\mathrm{e} = & -\frac{1}{B_0}\boldsymbol{b}\times\boldsymbol{\nabla}_\perp\Phi\cdot\boldsymbol{\nabla}T_\mathrm{e}\\ & -\frac{2}{3}T_\mathrm{e}\left[\left(\frac{2}{B_0}\boldsymbol{b}\times\boldsymbol{\kappa}\right)\cdot\left(\boldsymbol{\nabla}\Phi - \frac{1}{en_\mathrm{e0}}\boldsymbol{\nabla}P_\mathrm{e} - \frac{5}{2}\frac{k_\mathrm{B}}{e}\boldsymbol{\nabla}T_\mathrm{e}\right)\right.\\ & \left. + B_0\nabla_\parallel\left(\frac{V_{\parallel\mathrm{e}}}{B_0}\right)\right] + 0.71\frac{2T_\mathrm{e}}{3en_\mathrm{e0}}B_0\nabla_\parallel\left(\frac{J_\parallel}{B_0}\right)\\ & + \frac{2}{3n_\mathrm{e0}k_\mathrm{B}}\nabla_{\parallel 0}\left(\kappa_{\parallel\mathrm{e}}\nabla_{\parallel 0}T_\mathrm{e}\right) + \frac{2}{3n_\mathrm{e0}k_\mathrm{B}}\boldsymbol{\nabla}_\perp\cdot\left(\kappa_{\perp\mathrm{e}}\boldsymbol{\nabla}_\perp T_\mathrm{e}\right)\\ & - \frac{2m_\mathrm{e}}{m_\mathrm{i}}\frac{1}{\tau_\mathrm{e}}\left(T_\mathrm{e} - T_\mathrm{i}\right) + \frac{2}{3n_\mathrm{e0}k_\mathrm{B}}\eta_\parallel J_\parallel^2.\end{aligned} \tag{6}$$

The variables in these equations are defined as

$$\varpi = n_\mathrm{i0}\frac{m_\mathrm{i}}{B_0}\left(\nabla_\perp^2\phi + \frac{1}{n_\mathrm{i0}}\nabla_\perp\phi\cdot\nabla_\perp n_\mathrm{i0} + \frac{1}{n_\mathrm{i0}Z_\mathrm{i}e}\nabla_\perp^2 p_\mathrm{i1}\right), \tag{7}$$

$$J_\parallel = J_{\parallel 0} - \frac{1}{\mu_0}B_0\nabla_\perp^2\psi, \tag{8}$$

$$V_{\parallel\mathrm{e}} = V_{\parallel\mathrm{i}} + \frac{1}{\mu_0 Z_\mathrm{i}en_\mathrm{i}}\nabla_\perp^2 A_\parallel. \tag{9}$$

In this model, all the variables can be written as $F = F_0 + F_1$, where F_0 represents for the equilibrium part of arbitrary field quantity and F_1 is the perturbed component. Here $A_\parallel$ is the perturbed parallel vector potential, $\boldsymbol{b} = \boldsymbol{b}_0 + \boldsymbol{b}_1 = \boldsymbol{b}_0 + \boldsymbol{\nabla}A_\parallel \times \boldsymbol{b}_0/B$ is the unit vector of the total magnetic field, $\boldsymbol{\kappa} = \boldsymbol{b}_0\cdot\triangledown\boldsymbol{b}_0$. The definition of pressure in this model is $P_j = P_{j0} + p_{j1} = k_\mathrm{B}n_jT_j$, $p_{j1} = n_{j0}T_{j1} + n_{j1}T_{j0} + n_{j1}T_{j1}$ for j species. $\boldsymbol{V}_E = (\boldsymbol{b}_0\times\nabla_\perp\Phi)/B_0$, and $\Phi = \Phi_0 + \phi$ is the total electric potential. Note that $V_{\parallel\mathrm{i}}$, $V_{\parallel\mathrm{e}}$ and ϖ only have the perturbed part. Here $\Omega_\mathrm{i} = Z_\mathrm{i}eB/m_\mathrm{i}$ is the ion gyro frequency, $\nabla_\parallel = \nabla_{\parallel 0} - \boldsymbol{b}_0\times\boldsymbol{\nabla}A_\parallel/B_0$, $\boldsymbol{\nabla}_\perp = \boldsymbol{\nabla} - \boldsymbol{b}\nabla_\parallel$ and $\nabla_{\parallel 0} = \boldsymbol{b}_0\cdot\boldsymbol{\nabla}$.

The terms in two square brackets in equation (1) represent the gyro-viscous terms brought in by the finite ion Larmor radius (FLR) effects. These terms are necessary for the two-fluid models to keep the whole FLR stabilizing effects when ion density gradient is steep and temperature is high [18]. For this model, the net equilibrium zonal flow is set to be zero. If the net shear flow is not zero, it can stabilize high-n modes and introduce Kelvin–Helmholtz term to destabilize P–B modes, as discussed in [17]. The effects of turbulent zonal flow will be discussed in section 3.5.

This model is a simplification of the equations in the BOUT [20] code. The only difference is that the pressure is assumed to be isotropic here, so $\mu_{\parallel\mathrm{i}}\nabla_{\parallel 0}^2\varpi$ is the simple form of parallel viscosity and perpendicular viscosity is neglected in our model. In addition, the equations are written in SI units. η is defined as the parallel Spitzer resistivity, $\eta_\mathrm{SP} = 0.51 \times 1.03 \times 10^{-4}Z_\mathrm{i}\ln\Lambda T^{-3/2}\,\Omega\,\mathrm{m}^{-1}$. Although hyper-resistivity η_H, also known as electron viscosity, is generally negligibly small in collisional plasmas, it can be significant in a collisionless plasma. From nonlinear simulations we have found that the P–B modes trigger magnetic reconnection, which drives the collapse of the pedestal pressure. The hyper-resistivity is found to limit the radial spreading of ELMs by facilitating magnetic reconnection [15]. Either resistivity η or hyper-resistivity η_H can break the frozen-in flux constraint of ideal MHD theory.

The symbols $\kappa_{\parallel\mathrm{i}} = 3.9n_\mathrm{i}v_{\mathrm{th,i}}^2/\nu_\mathrm{i}$ and $\kappa_{\parallel\mathrm{e}} = 3.2n_\mathrm{e}v_{\mathrm{th,e}}^2/\nu_\mathrm{e}$ are Spitzer–Härm parallel thermal conductivities, where $v_{\mathrm{th},j}$ is the thermal velocity for j particle and ν_j is the collision rate. Since in the hot pedestal the collisionality is low and this classic $\kappa_{\parallel j}$ is not valid for the weakly collisional plasmas, the free-streaming expression $\kappa_{\mathrm{fs},j} = n_jv_{\mathrm{th},j}qR_0$, where q is the local safety factor, is taken into account of kinetic effects. Therefore, in the simulations the effective thermal conductivities are written as

$$\kappa_{\mathrm{eff},j} = \frac{\kappa_{\parallel j}\kappa_{\mathrm{fs},j}}{\kappa_{\parallel j} + \kappa_{\mathrm{fs},j}}. \tag{10}$$

Within this form, $\kappa_{\mathrm{eff},j}$ is determined by $\kappa_{\parallel j}$ at the bottom of the pedestal region where plasmas are in the collisional limit, and is dominant by $\kappa_{\mathrm{fs},j}$ in the high mean free path condition. The parallel diffusion terms should be evaluated along the total magnetic field lines. In practice this is challenging since $\kappa_{\parallel j}^{\mathrm{ef}} \gg \kappa_{\perp j}$ and $\kappa_{\parallel j}\nabla_{\parallel} \simeq 0$. For small δB perturbation, this is a reasonable approximation. Note that the perpendicular classical diffusivities are neglected here because in this typical P–B unstable equilibrium, $\kappa_{\perp} \ll \kappa_{\parallel}$. Therefore, we believe that the radial diffusion will not affect the simulation results in the linear phase and even in the early nonlinear phase, but in the late nonlinear phase, $\kappa_{\perp}$ may be important to transport and turbulent processes on the transport time scale.

Equations (1)–(9) are solved using the field aligned (flux) coordinate system (x, y, z) with the shift radial derivatives [13]. In this coordinate system x is the radial direction and is defined as $x = (\psi - \psi_{\mathrm{axis}})/(\psi_{\mathrm{separatrix}} - \psi_{\mathrm{axis}})$, which is the normalized poloidal flux and ψ is the poloidal magnetic flux, y is the parallel direction with a twisted-shift boundary condition and z is the bi-normal direction. Hereafter, we use $\Psi = x$ to represent the normalized magnetic flux for simplification. For conclusion, compared with the previous three-field model, this set of equations include the additional physics, such as ion acoustic waves, thermal conductivities, Hall effects, toroidal compressibility and electron–ion friction.

Compared with other similar models, for example, the electrostatic model in [21], our six-field model is electromagnetic so that it is able to simulate the magnetic reconnection triggered by P–B modes which leads to the pedestal collapse [12]. The finite Larmor radius effects are also taken into account in our model, which is neglected in [21]. Compared with the five-field model in [22], the evolutions of electron temperature and parallel thermal diffusivities are taken into consideration in our model because the parallel thermal diffusivity of electrons is fairly large to stabilize the P–B modes and constrain the radial spread of the perturbations [23]. The gyro-viscous terms in equation (1) are added into our model because it is necessary to be kept in the two-fluid model to represent the FLR effects. The parallel diffusion terms in the temperature equation due to the perturbed magnetic field are neglected in our model due to the perturbed magnetic field.

In this paper, we use two shifted circular cross-section toroidal equilibria with an aspect ratio of 2.9 generated by the TOQ code [25]. The parameters of both equilibria are minor radius $a = 1.17$ m, major radius $R_0 = 3.44$ m, magnetic field on axis $B_0 = 1.99$ T and $q_{95} = 2.57$. Equilibrium 1 has a normalized pressure gradient length scale $L_{\mathrm{p}}/a = 1.68\times10^{-2}$, a pedestal poloidal pressure $\beta_{\mathrm{t0}} = 1.92 \times 10^{-2}$, and a normalized pedestal width $L_{\mathrm{ped}}/a = 5.18\times10^{-2}$. On the other hand, equilibrium 2 has the parameter as $L_{\mathrm{p}}/a = 1.56 \times 10^{-2}$, $\beta_{\mathrm{t0}} = 1.94 \times 10^{-2}$ and $L_{\mathrm{ped}}/a = 4.86 \times 10^{-2}$. Equilibrium 2 is much more unstable than the first one for P–B modes. Both equilibria are ideal ballooning unstable. Equilibrium 2 has been well studied by the BOUT++ three-field model [12, 16, 17]. The MHD simulations without FLR effects on both cases are discussed in [26]. The definition of the plasma edge is somewhat arbitrary since here there is no scrape-off layer (SOL), and so $\Psi = 1$ is defined as the position where the equilibrium plasma pressure gradient and parallel current fall to zero.

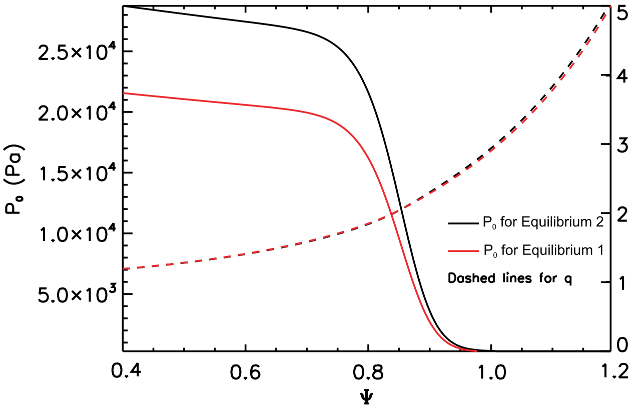

Figure 1. Profiles of background pressure P_0 and safety factor q of equilibria 1 and 2. The black solid curve is P_0 for equilibrium 2 and the red solid curve is for equilibrium 1. The black dashed curve is q for equilibrium 2 and the red dashed one is for equilibrium 1.

3. Simulation results and discussions

For both equilibrium mentioned in previous section, the equilibrium pressure profile P_0 (figure 1) is separated into ion density n_{i0}, ion and electron temperature, T_{i0} and T_{e0}. For the quasi-neutral condition, $Z_{\mathrm{i}}n_{\mathrm{i0}} = n_{\mathrm{e0}}$, where Z_{i} is ion charge and n_{e0} is equilibrium electron density. Here we assume $T_{\mathrm{i0}} = T_{\mathrm{e0}}$. In the analysis below, we choose the analytical profiles of n_{i0} as

$$n_{\mathrm{i0}}(x) = \frac{(n_{\mathrm{height}} \times n_{\mathrm{ped}})}{2}\left[1 - \tanh\left(\frac{x - x_{\mathrm{ped}}}{\Delta x_{\mathrm{ped}}}\right)\right] + n_{\mathrm{ave}} \times n_{\mathrm{ped}}, \tag{11}$$

here n_{ped} is the ion number density on the top of the pedestal region, n_{ave} is the ratio to control the bottom amplitude of n_{i0} outside the separatrix, and n_{height} is the coefficient to specify the gradient of n_{i0}. x_{ped} and Δx_{ped} represent the position of peak gradient and the width of the pedestal region of P_0, respectively. For both cases, we have $x_{\mathrm{ped}} = 0.633$ and $\Delta x_{\mathrm{ped}} = 0.1$. Note that if n_{i0} is outside $\Psi_n = 1$, the profile is set to be a constant value.

In the BOUT++ framework, the spatial discretizations are the finite differencing method in the x and y directions, and Fourier decomposition in the z direction. In this model, the fourth order central differencing method is adopted for first and second order derivatives. The third order WENO scheme [27] is applied for convective terms and the Arakawa scheme [28] is for the magnetic flutter term $\boldsymbol{b}_1 = -\nabla A_{\parallel} \times \boldsymbol{b}_0/B$. All the partial differential equations in the BOUT++ framework are solved via a method-of-lines approach and an implicit backward differencing scheme using a Newton–Krylov iteration to advance the system in time via a fully implicit Newton–Krylov solver PVODE [29]. In our simulations, the resolutions in the x and y directions are 516×64. For linear simulations, the grid number in the z direction is $n_z = 17$ in $1/n$ torus where n is the toroidal mode number. For nonlinear runnings $n_z = 65$ in one-fifth torus which is simulated.

3.1. Comparison with the three-field and five-field models

In the BOUT++ framework, a series of the two-fluid models have been developed to simulate ELM crashes within the

P–B model, such as the three-field [12] and five-field [23] model. The three-field two-fluid model, which evolves P, $A_\parallel$ and ϖ, is the simplest model to describe the P–B mode. Drift waves, ion-sonic waves, Hall MHD effects and magnetic pumping terms are all neglected. The five-field model is derived as the extension of the previous three-field two-fluid model for the reason of studying the effects of ion density and parallel thermal diffusivities during P–B modes. Therefore, the pressure equation is separated into ion density, ion and electron temperature equations. The effects of Spitzer–Härm thermal conductivities are also discussed in this model. Compared with these two models, this six-field model includes additional physics, such as drift waves, ion acoustic waves, Hall MHD effects, toroidal compressibility and ion–electron friction, thus this model can simulate both meso-scale MHD events and micro-scale drift-wave turbulence in collisional regimes.

In this comparison, both equilibrium 1 and equilibrium 2 are chosen. The density profile is chosen with the coefficients $n_{\rm ave} = 0.2$ and $n_{\rm height} = 0.55$ in equation (11) for equilibrium 2. Then the temperature has the value 1.2 keV at the pedestal top and 0.05 keV at the bottom. Figure 2(*a*) gives the comparison of the linear growth rate for this highly P–B unstable case. All three models show the similar instability island on toroidal mode number n range, from $n \sim 3$ or 5 to $n \sim 40$. The peak growth rates are also similar, especially for the three-field and six-field model. This difference is less than 10%. Compared with the five-field model, despite the fact that electron Hall effects can destabilize the P–B modes [16], both thermal conductivities [23] and gyro-viscous terms show effective stabilization. The other effects, such as thermal force and electron–ion friction, do not affect the linear growth rate significantly. The data in figure 2(*a*) is the same as that in table 1 of [18]. The differences of amplitude in the figure are due to the normalization. Here the normalization density $n_{i0} = 0.46 \times 10^{20}\,{\rm m}^{-3}$ is used in the calculation of Alfvén frequency ω_A as in ideal MHD simulations (the dashed-diamond curve in figure 2(*a*)). While in [18] the normalization density $n_{i0} = 10^{20}\,{\rm m}^{-3}$ is used. Figure 2(*b*) shows the linear growth rate comparison of the three-field and six-field models for equilibrium 1. The coefficients of density is chosen as $n_{\rm height} = 0.0728$ and $n_{\rm ave} = 0.04$. For the three-field model, as the black curve shows in panel (*b*), the instability island is narrower than the six-field model because the additional terms do enhance the instability in this marginal stable equilibrium, which is opposite to the highly unstable case, where other physics in the six-field model plays minimal roles to the linear growth.

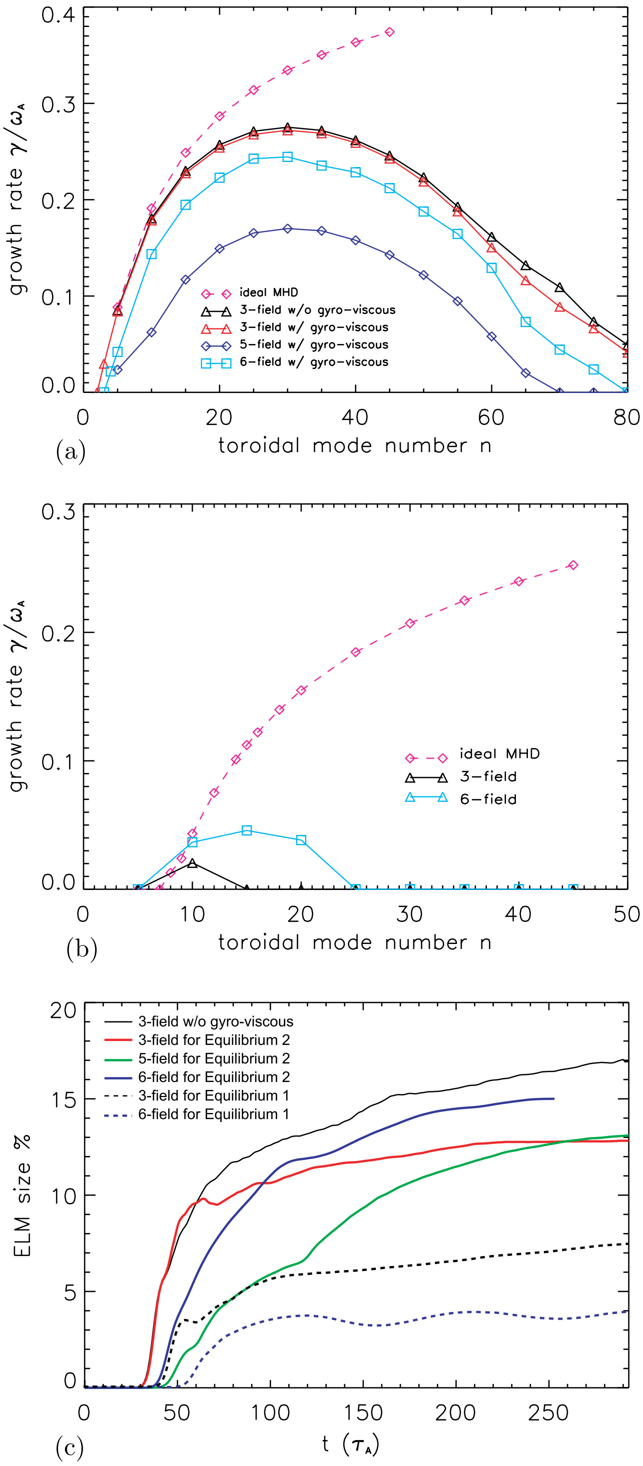

Figure 2. (*a*) Comparison of linear growth rate among our three-field, five-field and six-field model on strong unstable equilibrium 2. (*b*) Comparison of linear growth rate between three-field and six-field model on weak unstable equilibrium 1. (*c*) Time evolutions of ELM size among these models for both equilibria. For equilibrium 2, both three-field and six-field models show the consistent results at linear and nonlinear phases, while additional terms of six-field do enhance the instability in equilibrium 1. The six-field model yields smaller ELM size in both equilibria.

For nonlinear simulations, the gyro-viscous terms are added into both the three-field and five-field model because of its importance for two-fluid simulations [18]. In figure 2(*c*), the time evolution of ELM size for both equilibria 1 and 2 of the three-field, five-field and six-field model is shown. The ELM size here uses the same definition as in [12]. It is defined as $\Delta_{\rm ped}^{\rm th} = \Delta W_{\rm PED}/W_{\rm ped}$ and represents the ratio of the ELM energy loss $\Delta W_{\rm PED} = (3/2)\int_{R_{\rm in}}^{R_{\rm out}}\oint {\rm d}R\,{\rm d}\theta(P_0 - \langle P\rangle_\zeta)$ to the pedestal stored energy $W_{\rm ped} = (3/2)\int_{R_{\rm in}}^{R_{\rm out}}\oint {\rm d}R\,{\rm d}\theta\,P_0$. The symbol $\langle\rangle_\zeta$ means the average over the bi-normal periodic coordinate. The lower integral limit is the pedestal inner radial boundary $R_{\rm in}$, while the upper limit is the radial position of the peak pressure gradient $R_{\rm out}$. The ELM size can be calculated from each nonlinear simulation. The physics on the control of ELM size after the onset of each ELM (type-I) is still under investigation. In the previous studies, the ELM size is found to be weakly sensitive to the hyper-resistivity for large ELMs [18] and insensitive to the resistivity [12].

For a ballooning-dominated equilibrium the FLR effect can significantly decrease the ELM size when the pedestal ion temperature increases because high-n modes are stabilized [18]. In figure 2(*c*), the solid curves are for equilibrium 2 and the dashed curves are for equilibrium 1. The black solid curve is the three-field model without the gyro-viscous term and the red solid one is the same model with gyro-viscosity. The five-field model with gyro-viscous terms is drawn as the green solid curve and the six-field one as the blue solid curve. All these models show the similar time evolution that there is a slow increasing or saturation phase after the fast increase in ELM size. For the three-field model, the effects of gyro-viscous is significant and its ELM size is ∼2% less than the six-field model at the nonlinear saturation phase. The ELM size for the five-field model still exceeds the three-field one with gyro-viscosity, despite it having the smallest ELM size for most of the time. Although the six-field model includes so many additional effects compared with the original three-field model, the ELM size is just 11% less, which is the smallest difference among these models. For equilibrium 1, the P–B unstable case with $n_{\mathrm{ave}} = 0.2$ and $n_{\mathrm{height}} = 0.364$ are chosen here. As the dashed curves show in figure 2(*c*), the saturated ELM size of the six-field model is smaller than the three-field one. The absolute amount of the ELM size difference between the two models is around 3%, very similar to 2% of equilibrium 2.

Through these comparisons, we can see that although the equations of the six-field model are very different from the original three-field model, both linear and nonlinear activities of P–B instability are still close. This result indicates that the P–B instability, ion diamagnetic effects, resistivity and hyper-resistivity, which can be well described by our three-field model, are the dominant physics effects during the burst of ELMs. So the three-field model is good enough to simulate P–B instabilities and ELM crashes. The additional physics, such as ion acoustic waves, thermal conductivities, Hall effects, toroidal compressibility and electron–ion friction, are less important in this process. However, they are still very important and necessary to simulate the power depositions on the plasma-facing component, self-consistent turbulence and transport between ELMs for the rebuild of the pedestal, which is also the capability of this six-field model.

3.2. Linear simulations on equilibrium 1

For the purpose of studying ELM crashes, the turbulence and transport after that, equilibrium 1 is chosen for the following simulations. As introduced in section 2, this equilibrium is unstable for ideal P–B modes, as shown using the pink dashed curve in figure 3, but less unstable than the equilibrium 2 case. The six-field two-fluid simulations for this more unstable equilibrium case are described in [18]. The green dashed star curve is the linear growth rate derived from the ELITE code for the same equilibrium. The ideal instability occurs at the similar toroidal harmonics for both codes. BOUT++ also obtains the similar linear growth rate as ELITE at high toroidal mode number n. However, as shown by the black triangle curve in figure 3, this equilibrium is almost stable for P–B modes when $n_{\mathrm{i0}} = 10^{19}\,\mathrm{m}^{-3}$ without resistivity. Within six-field simulations, the similar temperature profiles are applied here as section 3.1, the temperature has the value 1.2 keV at the pedestal top. The density coefficients are chosen as $n_{\mathrm{ave}} = 0.2$ and $n_{\mathrm{height}} = 0.364$. The density at the pedestal top is $5.6 \times 10^{19}\,\mathrm{m}^{-3}$, which is larger than the value for the three-field simulations. It indicates that the diamagnetic stabilization is not strong enough to suppress the ideal P–B modes. The results are shown as the red triangle curve in figure 3. If the Spitzer resistivity is taken into account, the linear growth rate does not change, as shown by the blue diamond curve in figure 3. This indicates that this instability is really P–B modes, not resistive ballooning modes. The cyan square curve shows the growth rate derived by the six-field model with both Spitzer resistivity and hyper-resistivity. The hyper-Lundquist number is set to be a constant $S_{\mathrm{H}} = \mu_0 R_0 V_{\mathrm{A}}/\eta_{\mathrm{H}} = 10^{13}$, where V_{A} is Alfvén speed. This large S_{H} does not affect the linear growth rate, so the instability is not triggered by hyper-resistivity modes. In the following nonlinear simulations, this constant S_{H} will be applied.

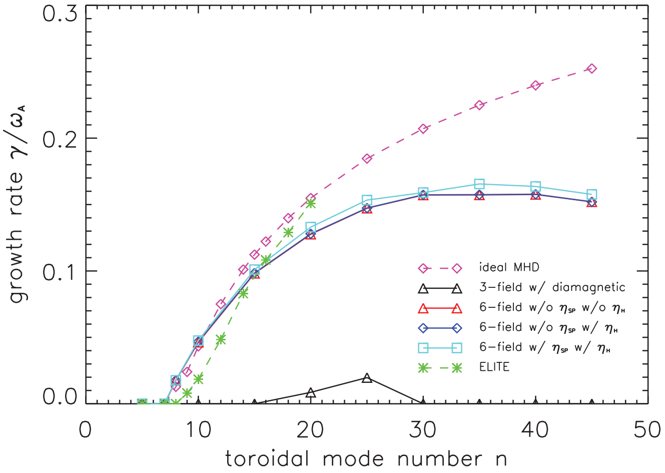

Figure 3. Linear growth rate for equilibrium 1. The three-field model with constant density shows this equilibrium is marginal stable. However, the six-field model shows that with certain density profile, this equilibrium is unstable for P–B modes.

3.3. Density scanning of nonlinear simulations

In this subsection, we simulate five different profiles of ion density, the coefficients are listed in table 1. These coefficients represent the different electron temperatures at the top of the pedestal. As shown in figure 4, all the cases with these coefficients are unstable except the $T_{\mathrm{e0,top}} = 9\,\mathrm{keV}$. The cases with $T_{\mathrm{e0}} = 3$, 1.2 and 0.6 keV are typical P–B modes and $T_{\mathrm{e0,top}} = 6\,\mathrm{keV}$ are dominated by marginal stable ballooning modes. The $T_{\mathrm{e0,top}} = 9\,\mathrm{keV}$ case is a small resistive ballooning mode since it is nearly stabilized by the strong ion diamagnetic effects. The equilibrium profiles of a different set of coefficients are plotted as the dashed curves in figure 5. Notice that all of these profiles are derived from the same equilibrium generated by the TOQ code. Both the pressure and current profiles are kept the same for all of these simulations.

The solid curves in figures 5(*a*)–(*c*) are the time-averaged radial profiles at the outer mid-plane during the saturation phase. In the saturation phase, the crash event of ELMs are finished and the profiles of densities, temperatures, current and parallel flow are in the quasi-steady state. Turbulence and transport are the dominant processes during this phase. The

Table 1. Coefficients of the five density profiles. $T_{\mathrm{e0,top}}$ is the equilibrium electron temperature at the pedestal top, and $n_{\mathrm{i0,top}}$ is the equilibrium ion density at this region.

	$T_{\mathrm{e0,top}}$ (keV)	$n_{\mathrm{i0,top}}/10^{20}$ (m^{-3})	n_{height}	n_{ave}
Case 1	9	0.08	0.0485	0.0267
Case 2	6	0.11	0.0728	0.04
Case 3	3	0.22	0.1456	0.08
Case 4	1.2	0.56	0.364	0.2
Case 5	0.6	1.13	0.728	0.4

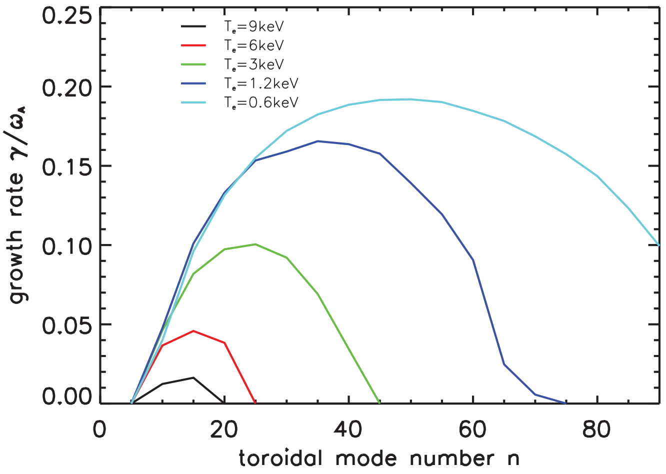

Figure 4. Linear growth rate versus toroidal mode number for the temperature scan.

evolution is so slow compared with the ELM crash event that it is very difficult to see the changes of the profiles on the Alfvén timescale. From figure 5, we can see that all the solid curves show a more gentle gradient than the dashed curves at the pedestal region. Such gentle gradients are not able to trigger P–B modes any more. These time-averaged profiles represent that of L-mode-like state between ELMs. If in the ELMy H-mode discharge, the right balance of sources and the turbulence and transport processes will lead to the slow rebuild of the steep gradient of the profiles after the collapse.

The parallel thermal diffusivity is defined as $\chi_{\parallel j} = \kappa_{\mathrm{eff},j}/(k_{\mathrm{B}}n_j)$. References [18, 23] show that thermal diffusivities are very effective at damping the perturbations at the pedestal top. In six-field simulations, we also get similar results. As shown in figure 6(*a*), the higher temperature leads to higher thermal velocity. At the top of the pedestal, the equilibrium is still in the low collisional limit, so the free-streaming of particles is dominant and this leads to a higher thermal diffusivity. The larger thermal diffusivity then leads to a larger damping effect at the top region. This effect also influences the ELM size. The black star curve in figure 6(*b*) gives the dependence of ELM size on the normalized separatrix density. In the figure, the normalized separatrix density is defined as $n_{\mathrm{sep}}/n_{\mathrm{G}}$ and the Greenwald density is $n_{\mathrm{G}} = I_{\mathrm{p}}/(\pi a^2)$. For all the cases plotted here, the instability is dominated by ballooning-dominant modes. Two factors can influence the value of ELM size. First, ELM size gets increased for higher density because of the smaller thermal diffusivity. Second, when $n_{\mathrm{sep}}/n_{\mathrm{G}}$ is low, the diamagnetic stabilization becomes stronger and suppresses the perturbations of high-n mode, while the high-n mode perturbations can lead to more energy loss during ELMs. The red, green and blue curves in figure 6(*b*) are ELM size for n_{i}, T_{i} and T_{e}, respectively, which is derived using the similar method as ELM size calculation in previous analysis. The ELM sizes on the ion channel become smaller when $n_{\mathrm{sep}}/n_{\mathrm{G}}$ is low, which are similar to the total one. From this figure we can see that energy loss during ELM is mainly contributed by ion temperature. The ion particle loss contributes the least to the total ELM size and it is also the least affected variable by the normalized density. Note that this simulation shows the opposite trend to experiments [30] because we use the same equilibrium which is dominated by ballooning modes. However, the bootstrap current will be

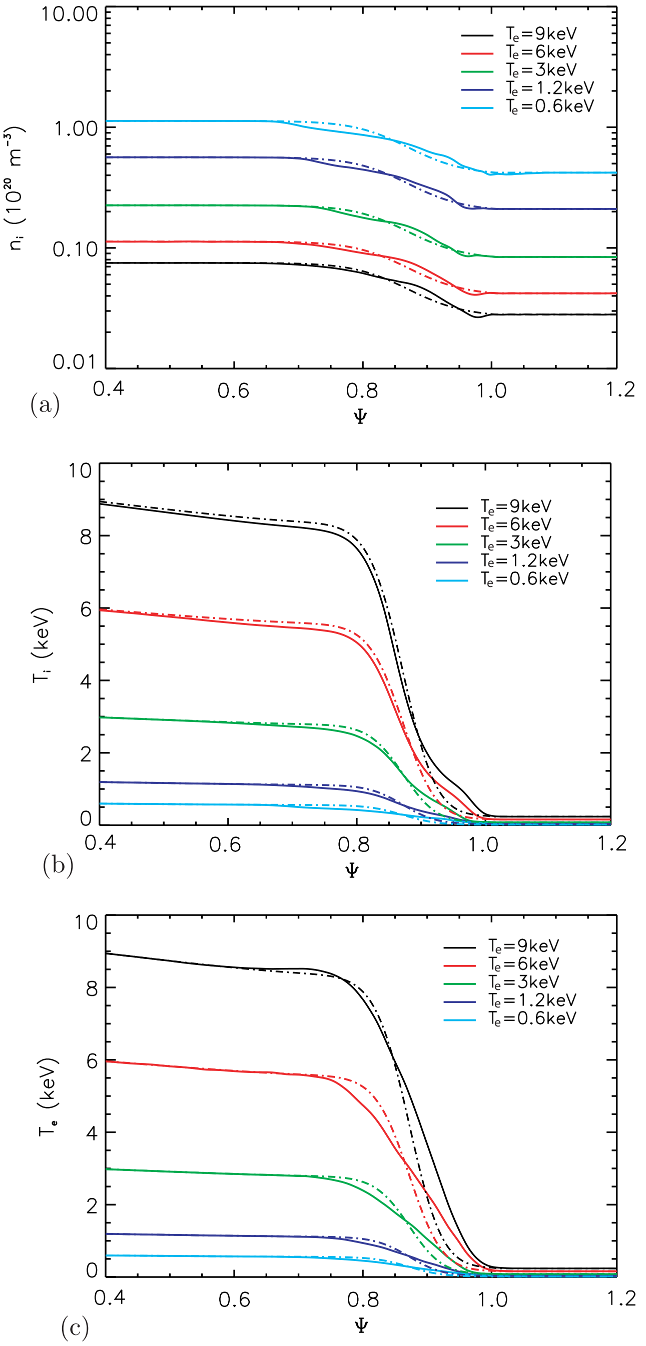

Figure 5. (*a*) Averaged ion density profiles at the saturation phase for the different cases. (*b*) Averaged ion temperature profiles. (*c*) Averaged electron temperature profiles. The dotted–dashed curves are the equilibrium profiles at the start of the simulations and the solid curves are the time-averaged profiles during the saturation phase.

much larger for the low $n_{\mathrm{sep}}/n_{\mathrm{G}}$ limit based on the Sauter formula [31, 32]. Such a large bootstrap current may trigger stronger peeling modes and lead to a larger ELM size.

3.4. Particle, heat flux and transport coefficients

One important capability of the six-field model is to study the self-consistent turbulence and transport between ELMs. In this subsection, the conductive radial ion density flux $\Gamma_{\mathrm{i}r}$ and radial heat flux $q_{\mathrm{i}r}$ are discussed. Their definitions are

$$\Gamma_{\mathrm{i}r} = \langle n_{\mathrm{i}} V_r \rangle = \left\langle n_{\mathrm{i}} \frac{(\boldsymbol{b}_0 \times \nabla\Phi)_r}{B_0} \right\rangle + \langle n_{\mathrm{i}} V_{\parallel \mathrm{i}} b_{1r} \rangle, \qquad (12)$$

$$q_{jr} = \langle T_j V_r \rangle = \langle n_j T_j \frac{(\boldsymbol{b}_0 \times \nabla\Phi)_r}{B_0} \rangle + \langle n_j T_j V_{\parallel j} b_{1r} \rangle. \qquad (13)$$

Here $\langle\rangle$ means flux surface average and $\langle f \rangle = 1/(2\pi)^2 \int_0^{2\pi} \mathrm{d}\phi \int_0^{2\pi} f \mathrm{d}\theta$. In these definitions the fluxes are constituted of two terms: the first term in equation (12) is the radial convective $\boldsymbol{E} \times \boldsymbol{B}$ drift and the second term is the non-zero averaged flux induced by the guiding centre motion along a magnetic field $\boldsymbol{B}$ which has an in-phase spatially fluttering radial magnetic component b_{1r} [33]. The comparison of $\Gamma_{\mathrm{i}r}$ with the different profiles listed in table 1 is shown in figure 7. Panel (*a*) gives the time evolutions of the density flux of ions at the peak pressure gradient position. Panel (*b*) shows the radial profiles of $\Gamma_{\mathrm{i}r}$. For the large ELM cases, as the cyan, blue, green and red curves show in panel (*a*), there are sharp peaks at the beginning of the nonlinear phase, which stands for the crashes of ELMs. The wider peak comes with the larger density case. However, no such obvious peaks are shown on black curves since the ELM size is very small. Both panels indicate that the radial particle flux almost has similar amplitudes at the peak pressure gradient position during the quasi-steady phase for all the cases.

We believe that the peak of the curve, which means the burst and crash of the particle flux in the radial direction, indicates a pump-out of ELM filaments. Figure 8 gives the time correlations between the ELM filaments and flux burst for the $T_{\mathrm{e}0} = 0.6\,\mathrm{keV}$ case. The upper figure is the time evolution of density profiles. There are two burst events of ELM filaments shown in this figure. The first one happens at $t = 160\tau_{\mathrm{A}}$ and the second one is at $t = 250\tau_{\mathrm{A}}$. These two filaments are labelled by the black dashed curves. Meanwhile, the radial particle flux at the pressure peak gradient region with $\Psi = 0.855$, as the lower panel of figure 8, also shows the burst events at the same time. The first peak is related to the first filament event and the third one is with the second filament. From this figure, we can say that the first filament is the major burst. The third peak is much smaller than the first one, thus the second filament is a micro-burst. The second peak of the particle flux is correlated with the disappearance of the filament which happens at $t = 190\tau_{\mathrm{A}}$. After $t = 250\tau_{\mathrm{A}}$, there is nearly no obvious peak for the particle flux, the whole system goes into the saturation phase and the density profile acts like that of L-mode. There are no ELM filaments burst and turbulence transport is the dominant physics in this phase.

The time evolutions of the radial heat flux of ions $q_{\mathrm{i}r}$ at the peak pressure gradient position are shown in figure 9(*a*), and those for q_{er} are shown in panel (*c*). Panels (*b*) and (*d*) are the radial profiles of flux averaged $q_{\mathrm{i}r}$ and q_{er}. In figure 9, we can see that the higher temperature cases show larger radial heat flux, especially at the saturation phase, while this trend is not obvious at the crash phase. The radial profiles indicate that both $q_{\mathrm{i}r}$ and q_{er} are peaked at the temperature peak gradient region, which is at the range around normalized $\Psi = 0.855$. At the inner side of the peak gradient region, the heat flux is almost one order of magnitude smaller. q_{jr} decreases quickly in the SOL region where $\psi > 1$ because the profiles here are all flat and no source can drive the radial transport. The second peaks for the heat fluxes are found at $\Psi = 0.5$ in figures 9(*b*) and (*d*) where there is a peak of ion temperature gradient (ITG). Therefore, this peak is driven by the ITG turbulence. Further analysis indicates that the perturbations ϕ and $T_{\mathrm{i}1}$ are 90 degrees out-phase and show the drift-like behaviours. The second peaks on electron heat fluxes are caused by the same reason because we use the same $\boldsymbol{E}\times\boldsymbol{B}$ drift and $T_{\mathrm{e}0} = T_{\mathrm{i}0}$ in the calculations.

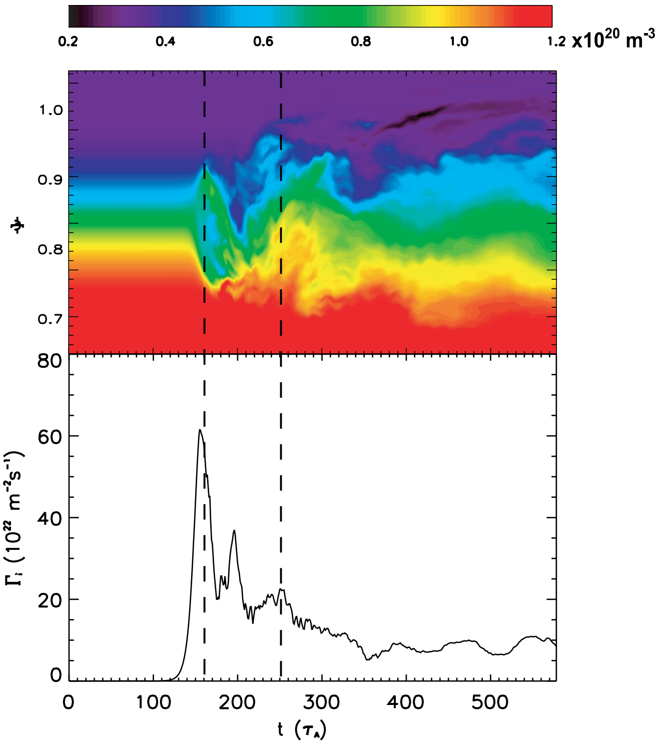

Figure 8. Relation between ELM filaments blow-up and particle flux for $T_{\mathrm{e}0} = 0.6\,\mathrm{keV}$. The upper figure is the time evolution of the radial profile of n_{i} at the outer mid-plane. The unit is $10^{20}\,\mathrm{m}^{-3}$. The lower figure is the time evolution of Γ_{i} at the density peak gradient region. Two dashed curves show that the first ELM burst is correlated with the first peak of Γ_{i} and the latter micro-burst is also correlated with the peak of Γ_{i}.

In the integrated modelling for plasma profile evolutions, the radial transport coefficients are considered to be very important in the process of rebuilding the pedestal. This six-field model can obtain these coefficients in the saturation phase after ELM crashes. The transport coefficients of particle flux D_r is defined as

$$D_r = -\frac{\Gamma_{\mathrm{i}r}}{\langle \frac{\partial n_{\mathrm{i}}}{\partial r} \rangle}, \qquad (14)$$

where the denominator is the radial derivative of the flux surface average of density and r is the minor radius. The ion

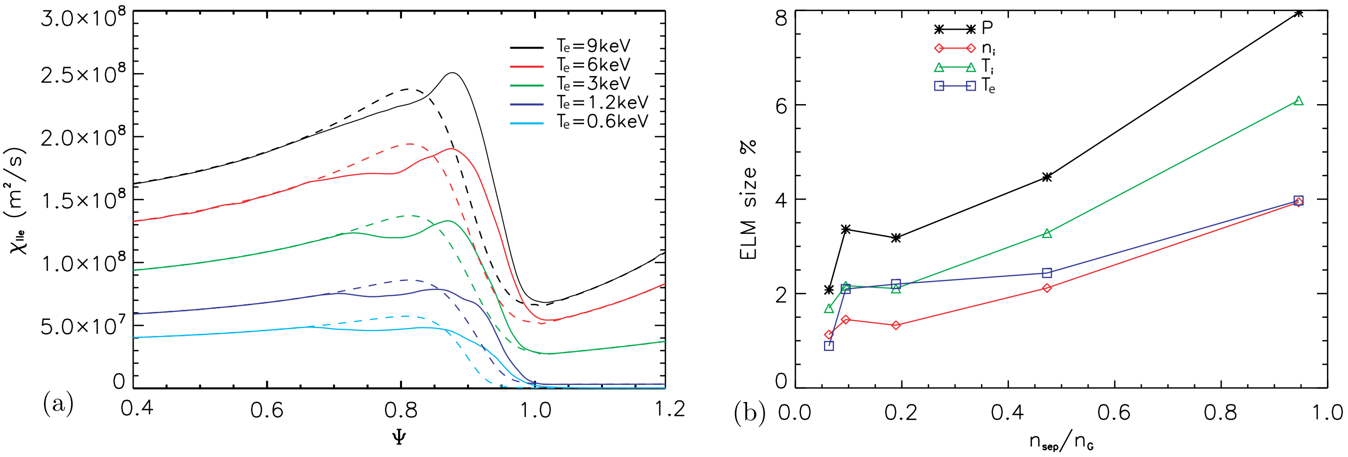

Figure 6. (*a*) Radial profiles of parallel electron thermal diffusivities $\chi_{\parallel e}$ for different cases. The dashed curves are the initial parallel thermal diffusivities at the start of the simulations and the solid curves are the time averaged $\chi_{\parallel e}$ during the saturation phase. (*b*) ELM size dependence on the normalized density for different channels. The black star curve is the total ELM size. The red diamond is for ion density loss ratio, the green triangle is ion temperature loss ratio and the blue square is electron temperature. The overall trends show that the ELM size becomes larger when $n_{\rm sep}/n_{\rm G}$ increases.

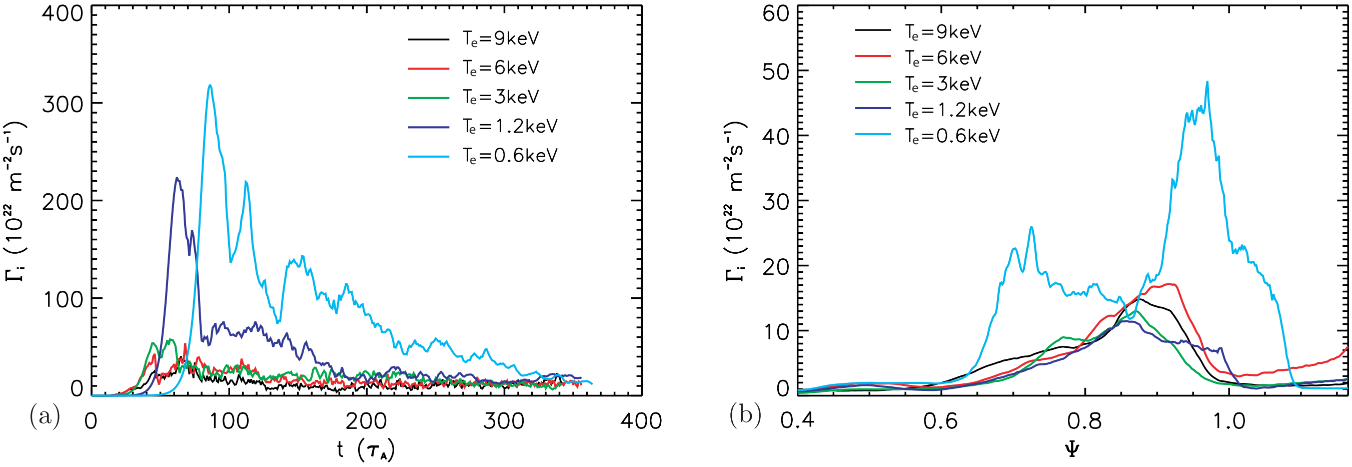

Figure 7. (*a*) Time evolution of the particle flux of ions at the peak pressure gradient position. (*b*) Radial profiles of particle flux of ions at the saturation phase. Both panels indicate that the radial particle flux is larger at the pressure peak gradient region when temperature is low or $n_{\rm sep}/n_{\rm G}$ is high.

and electron radial heat transport coefficients $\chi_{\rm ir}$ and $\chi_{{\rm e}r}$ are written as

$$\chi_{jr} = -\frac{q_j}{\langle \frac{\partial T_j}{\partial r} \rangle}. \tag{15}$$

The radial profiles for $\chi_{\rm ir}$ and $\chi_{{\rm e}r}$ are shown in figure 10(*a*) and (*b*). In the figures, all the transport coefficients change their sign at $\Psi = 0.82$, where the second-order derivative of pressure or the negative perturbation of P–B modes gets its extreme value. Inside this point, the perturbations propagate to the core region, while the fluxes change their directions to the SOL region outside this point. Such effects will lead to the more gentle profiles of the pedestal region. However, compared with the parallel thermal diffusivities shown in figure 6(*a*), these transport coefficients are much smaller. The timescale for this radial transport is $T_{Dr} \simeq a^2/D_r \sim 0.001$ s, which is much larger than Alfvén time $\tau_{\rm A} = 1.12 \times 10^{-6}\,{\rm s}^{-1}$. Therefore, it is very difficult to see such slow transport behaviours in the Alfvén timescale and the status of the system is in the quasi-steady state.

Figure 11(*a*) shows the relation between the fluxes and normalized density. The dashed curves are time averaged during the ELM crash phase and the solid curves are at the saturation phase. The definition of the period of the ELM crash phase is the time interval of the largest two peaks on the time tracing plots of the fluxes in figures 7 and 9, and the saturation phase is defined as the period that the amplitudes of the particle fluxes just oscillate around a certain value and do not show any sudden changes. The time interval for different cases are listed in table 2. For $\Gamma_{{\rm i}r}$, its amplitude is larger when the ratio $n_{\rm sep}/n_{\rm G}$ is higher at the ELM crash phase, while at the saturation phase, the amplitudes of $\Gamma_{{\rm i}r}$ drop dramatically for large density. This drop effect is not obvious for the small density case. As shown by the analysis in figure 8, the radial particle flux here is related to the particle loss during ELMs. For the larger density case at the ELM crash phase, the amplitude of $\Gamma_{{\rm i}r}$ is larger and the time interval of the ELM crash phase is also longer, as shown in figure 7(*a*). Therefore, more particle loss is induced by both larger $\Gamma_{{\rm i}r}$ and longer time. Although at the saturation phase, the amplitudes of $\Gamma_{{\rm i}r}$ drop to be comparable for all density cases, the time integral of the particle loss still leads to the larger ELM size in the particle channel. The blue and red curves show the change in heat flux for ions and electrons.

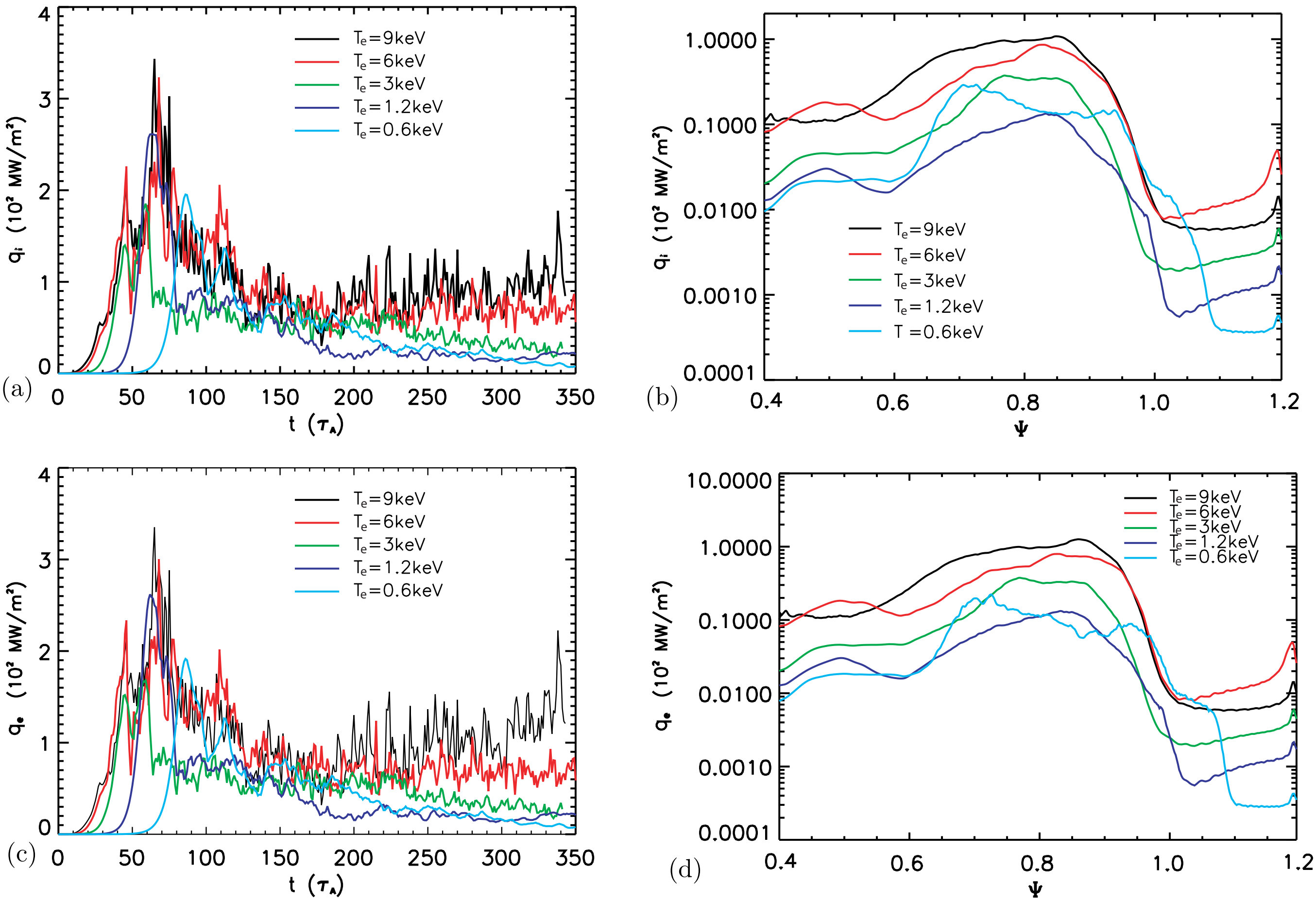

Figure 9. (*a*) Evolution of the radial heat flux of ions q_{ir} at the peak pressure gradient position. (*b*) Radial profile of q_{ir} at the saturation phase. (*c*) Evolution of the radial heat flux of electrons q_{er} at the peak pressure gradient position. (*d*) Radial profile of flux averaged q_{er} at the saturation phase. The larger temperature cases show larger radial heat flux.

Similar to Γ_{ir}, the amplitudes of q_{jr} also decrease a lot for high densities and drop little for low densities. Based on the transport equation of energy, the ELM size for the temperature channel can be written as

$$\frac{\int_{R_{\rm in}}^{R_{\rm out}} \oint \mathrm{d}R\,\mathrm{d}\theta (T_{j0} - \langle T_j \rangle_\zeta)}{\int_{R_{\rm in}}^{R_{\rm out}} \oint \mathrm{d}R\,\mathrm{d}\theta T_{j0}} \simeq \frac{\int \mathrm{d}t \left[\oint \mathrm{d}S(\langle q_{jr} \rangle_\zeta - q_{jr}^0) \right]}{\int_{R_{\rm in}}^{R_{\rm out}} \oint \mathrm{d}R\,\mathrm{d}\theta T_{j0}}. \tag{16}$$

At the ELM crash phase, the heat fluxes nearly do not change with density, so the energy loss during the same time interval are comparable for different cases. However, the higher density leads to lower temperature in the pedestal region since the pressure is fixed for the scan, so the ratio of energy loss for higher density is also larger because of the lower temperature T_{j0} in the denominator.

The dependence of transport coefficients on the ratio $n_{\rm sep}/n_{\rm G}$ is shown in figure 11(*b*). The black triangle curve is the particle transport coefficients D_r. The red and blue diamond curves are for χ_{ir} and χ_{er}, respectively. The dashed curves are time averaged during the ELM crash phase and the solid curves are at the saturation phase. The values are all measured at the pressure peak gradient region. This figure shows that these transport coefficients have similar trends at the ELM crash phase. When the ratio $n_{\rm sep}/n_{\rm G}$ is high, which means the high density cases and large P–B unstable ELMs, the coefficients are larger, which shows the same trend as the ELM size in figure 6(*b*). Similar to the particle and heat fluxes, the amplitudes of the coefficients also decrease dramatically at high-density cases. Compared with $\chi_{\rm ir}$ and $\chi_{\rm er}$, at the ELM crash phase, we can see $\chi_{\rm ir} > \chi_{\rm er}$. This indicates the larger energy loss through the ion channel, which is consistent with the ELM size, figure 6(*b*). At the saturation phase, although we have $\chi_{\rm ir} < \chi_{\rm er}$, the value is much smaller and most of the energy loss has already happened at the ELM crash phase. Therefore, the ELM size is mainly determined by the energy loss at the crash phase, the contribution of the quasi-steady state after the ELM crash is much smaller. The reason why $D_{\rm ir}$ is much larger than χ_{jr} is because the gradient of density is much more gentle than temperatures, and the scale length of the density to temperature is $L_n/L_{Ti} \simeq 5$ in our simulations. At the saturation phase, the typical values for transport coefficients at the saturation phase are $D_r \sim 200\,\mathrm{m^2\,s^{-1}}$, $\chi_{ir} \sim \chi_{er} \sim 40\,\mathrm{m^2\,s^{-1}}$.

3.5. *Turbulent zonal flow during ELMs*

In this section we investigate the role of zonal flow during and after ELM crashes. As shown in figure 12, the time evolutions of the kinetic energy $E_{\rm k}$ and the magnetic energy $E_{\rm m}$ are plotted for two cases listed in table 1. Case 4 represents a typical large ELM case and case 1 is a small one. Here the definition of the

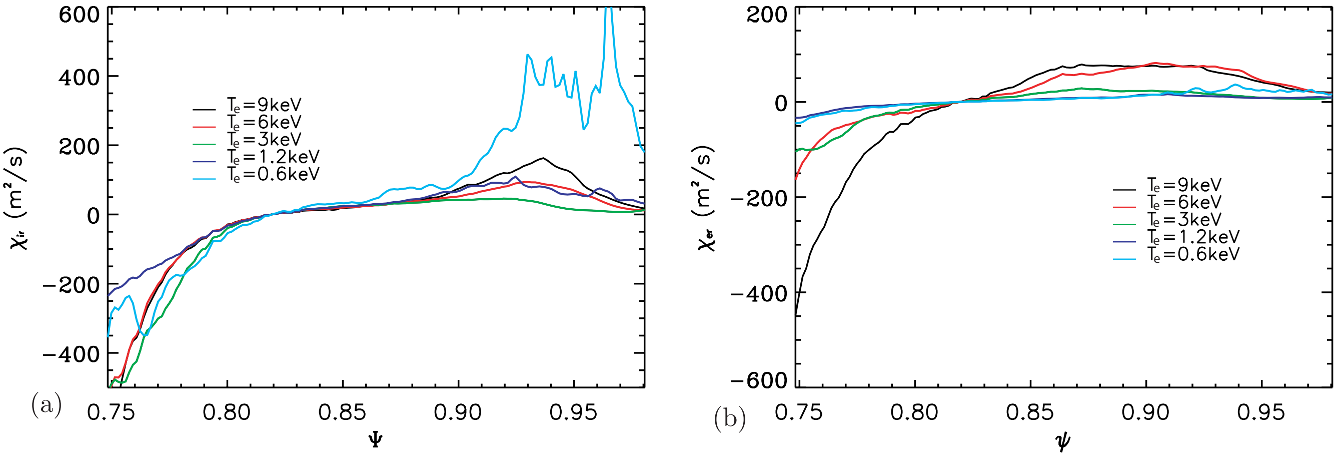

Figure 10. (*a*) Radial profiles of ion heat flux transport coefficients χ_{ir} for different cases listed in table 1. (*b*) Radial profiles for the electron heat flux transport coefficients χ_{er}.

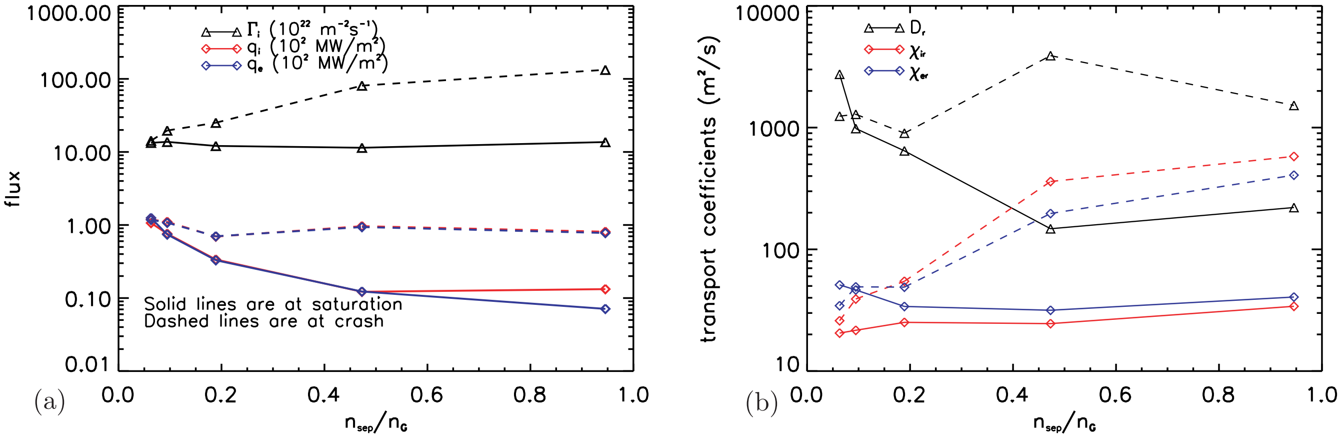

Figure 11. (*a*) Amplitude of the particle flux Γ_{ir} and the heat flux q_{jr} versus normalized density. (*b*) Radial transport coefficients of particle flux D_r, heat flux χ_{ir} and χ_{er} versus $n_{\rm sep}/n_{\rm G}$. The black triangle curve is for D_r, the red diamond is for χ_{ir} and the blue diamond is for χ_{er}. All the values are measured at the pressure peak gradient region where $\psi = 0.855$. In both panels, the dashed curves are time averaged at the ELM crash phase and the solid curves are at the saturation phase.

energy is given by

$$E_{\rm k} = \int {\rm d}\boldsymbol{x}^3 \frac{V_E^2}{2}, \qquad (17)$$

$$E_{\rm m} = \int {\rm d}\boldsymbol{x}^3 \frac{B_1^2}{2\mu_0}. \qquad (18)$$

Figure 12(*a*) shows the time evolutions of the different mode n of $E_{{\rm k}(n)}$ for case 4. The $n = 0$ mode shows the much larger amplitude than the other modes. It indicates that in this large ELM case, the zonal flow is the dominant part and regulates the turbulence for the whole simulation time. For other modes, the blue curve, which stands for the $n = 15$ mode, is the initial perturbation for nonlinear simulations and it is dominant at the linear growing phase. Then the nonlinear mode coupling induces the rapid increase in the other modes. The zonal flow appears a little earlier than the high-n modes from $t \simeq 14\tau_{\rm A}$, while the other high-n modes appear in the figure from $t \simeq 30\tau_{\rm A}$. From $t \simeq 60\tau_{\rm A}$, $E_{\rm k}$ of the $n = 15$ mode start to become comparable to other induced modes except the zonal flow. The energy amplitudes of these high-n modes are nearly one magnitude order lower than the zonal energy, which balances the zonal ion diamagnetic flow because of the zonal vorticity being set to zero ($\langle\varpi\rangle = 0$) for our ELM simulations.

Table 2. Time interval of ELM crash and saturation phase for different cases in table 1.

Time interval	ELM crash ($\tau_{\rm A}$)	Saturation ($\tau_{\rm A}$)
Case 1	60–80	250–end
Case 2	40–80	250–end
Case 3	30–70	250–end
Case 4	40–80	250–end
Case 5	70–130	330–end

Figure 12(*b*) is the time traces of $E_{{\rm k}(n)}$ for case 2 with small ELM. Different from case 4, the zonal kinetic energy regulates the turbulence only at the early nonlinear phase, from $t \simeq 40\tau_{\rm A}$ to $250\tau_{\rm A}$. In this case, the appearance of the induced modes are earlier than case 4. The zonal flow grows almost at the beginning of the simulation and the high-n induced modes appear from $t \simeq 10\tau_{\rm A}$. After $t \simeq 250\tau_{\rm A}$, all the high-n modes show comparable amplitudes with zonal flow.

Based on [34], the definition of the energy transfer to the zonal flow is obtained from the nonlinear (0, 0) Fourier component of equation (1) as

$$\frac{\rm d}{{\rm d}t}\int {\rm d}\boldsymbol{x} m_{\rm i} n_{\rm i0}\frac{V_{E00}^2}{2} = T_{00}^{\rm R} + T_{00}^{\rm ID} + T_{00}^{\rm M} + T_{00}^{\rm C}, \qquad (19)$$

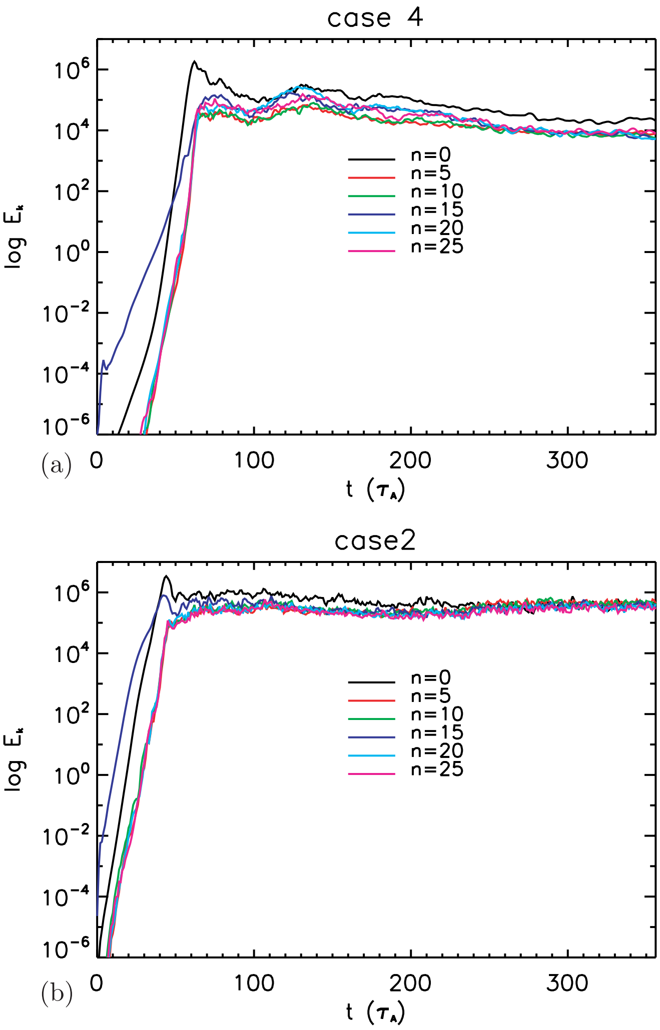

Figure 12. (*a*) Time traces of the kinetic energy $E_{k(n)}$ for each toroidal mode n of case 4 in table 1. The zonal flow dominates the turbulence from the start of nonlinear phase. (*b*) Time traces of the kinetic energy $E_{k(n)}$ for each toroidal mode n of case 2. The zonal flow only dominates the turbulence at the early nonlinear phase.

where

$$T_{00}^{\mathrm{R}} = -\int \mathrm{d}\boldsymbol{x}\phi_{00}\left(\frac{1}{B_0}\boldsymbol{b}\times\boldsymbol{\nabla}_\perp\phi\cdot\boldsymbol{\nabla}U'\right)_{00}, \tag{20}$$

$$T_{00}^{\mathrm{ID}} = -\int \mathrm{d}\boldsymbol{x}\phi_{00}\frac{m_{\mathrm{i}}}{B_0 Z_{\mathrm{i}} e}\left[\frac{1}{B_0}\boldsymbol{b}\times\boldsymbol{\nabla}_\perp\phi\cdot\boldsymbol{\nabla}\left(\nabla_\perp^2 p_{\mathrm{i}1}\right)\right]_{00}, \tag{21}$$

$$T_{00}^{\mathrm{M}} = -\int \mathrm{d}\boldsymbol{x}\phi_{00}\left[B_0^2\nabla_\parallel\left(\frac{\nabla_\perp^2\psi}{\mu_0}\right)\right]_{00}, \tag{22}$$

$$T_{00}^{\mathrm{C}} = \int \mathrm{d}\boldsymbol{x}\phi_{00}\left(2\boldsymbol{b}\times\boldsymbol{\kappa}\cdot\boldsymbol{\nabla}p_{\mathrm{i}1}\right)_{00} \tag{23}$$

are the contribution to Reynolds stress, the ion diamagnetic term, Maxwell stress and the curvature term. Note that $U' = n_{\mathrm{i}0}\frac{m_{\mathrm{i}}}{B_0}\nabla_\perp\phi + \frac{m_{\mathrm{i}}}{B_0}\nabla_\perp\phi\cdot\nabla_\perp n_{\mathrm{i}0}$ is defined as the vorticity without ion diamagnetic drifts. Note that the contribution of the gyro-viscous terms is not included in this discussion. The time evolutions of the energy transfer to zonal flow is plotted in figure 13. Panel (*a*) is about the P–B unstable case 4 and panel (*b*) shows case 2 with small ELMs. In both cases, the Reynolds stress T_{00}^{R} is positive and drives the flow during the whole process of our simulations, while the ion diamagnetic term and curvature term are negative and suppress the growing of the zonal flow. In panel (*a*), the Maxwell stress drives the flow just before $t \simeq 70\tau_{\mathrm{A}}$ and then becomes negative. The cyan curve in figure 13 indicates that the total contribution of the Reynolds stress and the ion diamagnetic term mainly drives the zonal flow after $t \simeq 70$. The total effects of these four terms suppress the zonal flow especially from $t \sim 60\tau_{\mathrm{A}}$ to $130\tau_{\mathrm{A}}$, as the purple curve shows, and this is the reason why the kinetic zonal energy $E_{\mathrm{k}(0)}$ decreases dramatically after ELM crashes at this period, as shown in figure 12(*a*). For panel (*b*), the total contribution of the four terms are just oscillating around 0 from $t \simeq 100\tau_{\mathrm{A}}$. Only a short period of negative value can be found from $t \sim 50\tau_{\mathrm{A}}$ to $70\tau_{\mathrm{A}}$, which is correlated with the small decrease in $E_{\mathrm{k}(0)}$ at the early nonlinear phase, as the black curve shows in figure 12(*b*).

4. Summary

In this paper we develop the six-field two-fluid model under the BOUT++ framework from Braginskii equations. The first-part work for the strong unstable case is to benchmark with the previous three-field and five-field two-fluid model in BOUT++. Although there are several additional physics, such as ion acoustic waves, thermal conductivities, Hall effects, toroidal compressibility and electron–ion friction, in this six-field model, they do not qualitatively change the linear instability properties and early phases of ELM dynamics. The dominant physics in ELMs are P–B instability, ion diamagnetic effects, resistivity and hyper-resistivity, which can be well described by the three-field model. Therefore, the three-field model is good enough to simulate ELMs. However, the six-field two-fluid model is still very important and necessary to simulate the power depositions on the plasma-facing component, self-consistent turbulence and transport between ELMs for the rebuilding of the pedestal.

The second part focuses on equilibrium 1. This equilibrium can be stable for P–B modes when ion diamagnetic effects are strong enough for low ion density. We simulated five different initial temperature profiles with the same pressure and current profiles under this equilibrium. Three cases, cases 3, 4 and 5 are P–B unstable, case 2 is destabilized by the additional terms and case 1 is the resistive ballooning turbulence. Our simulations show that the ELM size is smaller for the low density case. The ion channel contributes most to the total ELM size and the particle loss of ions contributes the least.

The third part is about the radial transport in the saturation phase after ELM crashes. The radial particle flux $\Gamma_{\mathrm{i}r}$ is closely related to the formation of ELM filaments. In our simulation, the first peak of $\Gamma_{\mathrm{i}r}$ represents the burst of ELM filaments. The second peak means the disappearance of filaments. The third peak indicates the micro-burst of filaments after the first strong one. After these three peaks, there are nearly no peaks in $\Gamma_{\mathrm{i}r}$ and the system goes to saturation. The radial transport coefficients at the ELM crash phase show good agreement with the ELM size on each channel. This indicates that the ELM size is mainly determined by the energy loss at the crash phase, the contribution of the quasi-steady state after the ELM crash is negligible. During the saturation phase, the typical values for radial transport coefficients are $D_r \sim 200\,\mathrm{m}^2\,\mathrm{s}^{-1}$,

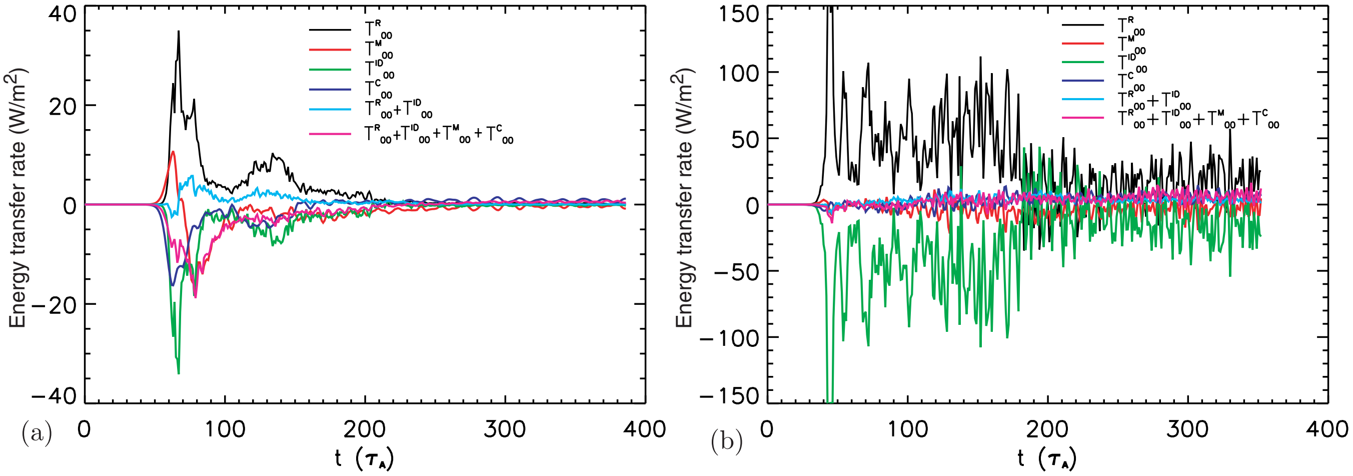

Figure 13. (*a*) Evolutions of energy transfer to zonal flow by the Reynolds stress T^{R}_{00} (black curve), the ion diamagnetic term T^{ID}_{00} (green), the Maxwell stress T^{M}_{00} (red) and the toroidal curvature T^{C}_{00} (blue) in the vorticity equation of case 4. The cyan curve is the total contribution of T^{R}_{00} and T^{ID}_{00} and the purple one is for the total of all four terms. (*b*) The evolutions of energy transfer to the zonal flow for the small ELM case 2. The vertical axes is the energy transfer rate (W/m^2).

$\chi_{ir} \sim \chi_{er} \sim 40\,\mathrm{m}^2\,\mathrm{s}^{-1}$ in the range of $n_{\mathrm{sep}}/n_{\mathrm{G}}$ as discussed in this paper.

The turbulent zonal flow regulates the turbulence from the ELM crash phase to the nonlinear quasi-steady states for large ELM cases; while for small ELM cases, the turbulent zonal flow is just dominant at the early nonlinear phase. The energy transfer analysis shows that the Reynolds stress is the main driving force to the zonal flow, and the ion diamagnetic drifts are the main suppressing force.

Acknowledgments

The authors wish to thank Drs B.D. Dudson and M.V. Umansky for their contributions to the BOUT++ framework, Drs P.H. Diamond, D. Dimits and I. Joseph for useful physics discussions. This work was performed under the auspices of the US DoE by LLNL under Contract DE-AC52-07NA27344 and is supported by the China NSF under Contract No 10721505, the National Magnetic Confinement Fusion Science Programme of China under Contracts No 2011GB107001 and National ITER plans Programme of China No 2011GB105003. LLNL-JRNL-610773.

References

[1] Doyle E.J. *et al* 2008 *22nd IAEA Fusion Energy Conf.(Geneva, Switzerland, September 2008)* CD ROM file EX/1-3

[2] Keilhacker M. *et al* 1984 *Plasma Phys. Control. Fusion* **26** 49

[3] Snyder P.B. *et al* 2009 *Nucl. Fusion* **49** 085035

[4] Snyder P.B., Wilson H.R., Ferron J.R., Lao L.L., Leonard A.W., Osborne T.H., Turnbull A.D., Mossessian D., Murakami M. and Xu X.Q. 2002 *Phys. Plasmas* **9** 2037

[5] Wilson H.R., Snyder P.B., Huysmans G.T.A. and Miller R.L. 2002 *Phys. Plasmas* **9** 1277

[6] Bernard L.C., Helton F.J. and Moore R.W. 1981 *Comput. Phys. Commun.* **24** 377

[7] Sovinec C.R., Glasser A.H., Gianakon T.A., Barnes D.C., Nebel R.A., Kruger S.E., Schnack D.D., Plimpton S.J., Tarditi A. and Chu M.S. 2004 *J. Comput. Phys.* **195** 355

[8] Brennan D.P., Kruger S.E., Schnack D.D., Sovinec C.R. and Pankin A. 2006 *J. Phys.: Conf. Ser.* **46** 63

[9] Snyder P.B., Wilson H.R. and Xu X.Q. 2005 *Phys. Plasmas* **12** 056115

[10] Snyder P.B., Wilson H.R. and Xu X.Q. 2006 Nonlinear 3D simulations of ELMs with the BOUT code *Fluid Modelling of ELMs Workshop (Boulder, CO, 2006)*

[11] Huysmans G.T.A. and Czarny O. 2007 *Nucl. Fusion* **47** 659

[12] Xu X.Q., Dudson B.D., Snyder P.B., Umansky M.V. and Wilson H.R. 2010 *Phys. Rev. Lett.* **105** 175005

[13] Dudson B.D., Umansky M.V., Xu X.Q., Snyder P.B. and Wilson H.R. 2009 *Comput. Phys. Commun.* **180** 1467

[14] Dudson B.D., Xu X.Q., Umansky M.V., Wilson H.R. and Snyder P.B. 2011 *Plasma Phys. Control. Fusion* **53** 054005

[15] Xu X.Q., Dudson B.D., Snyder P.B., Umansky M.V., Wilson H. and Casper T. 2011 *Nucl. Fusion* **51** 103040

[16] Xia T.Y., Xu X.Q., Dudson B.D. and Li J. 2012 *Contrib. Plasma Phys.* **52** 353

[17] Xi P.W., Xu X.Q., Wang X.G. and Xia T.Y. 2012 *Phys. Plasmas* **19** 092503

[18] Xu X.Q. *et al* 2013 *Phys. Plasmas* **20** 056113

[19] Xu X.Q., Cohen R.H., Rognlien T.D. and Myra J.R. 2000 L–H transitions simulations in divertor geometry *Phys. Plasmas* **7** 1951–8

[20] Xu X.Q., Umansky M.V., Dudson B.D. and Snyder P.B. 2008 *Commun. Comput. Phys.* **4** 949

[21] Scott B. 1997 *Plasma Phys. Control. Fusion* **39** 471

[22] Ishizawa A. and Nakajima N. 2007 *Phys. Plasmas* **14** 040702

[23] Xia T.Y. and Xu X.Q. 2013 *Phys. Plasmas* **20** 052102

[24] Hastie R.J., Ramos J.J. and Porcelli F. 2003 *Phys. Plasmas* **10** 4405

[25] Miller R.L. and Dam J.W.V. 1987 *Nucl. Fusion* **27** 2101

[26] Burke B.J., Kruger S.E., Hegna C.C., Zhu P., Snyder P.B., Sovinec C.R. and Howell E.C. 2010 *Phys. Plasmas* **17** 032103

[27] Liu X.D., Osher S. and Chan T. 1994 *J. Comput. Phys.* **115** 200

[28] Arakawa A. 1966 *J. Comput. Phys.* **1** 119

[29] Cohen S.D. and Hindmarsh A.C. 1996 *Comput. Phys.* **10** 138 Byrne G.D. and Hindmarsh A.C. 1999 *Int. J. High Perfm. Comput. Appl.* **13** 354

[30] Leonard A.W. *et al* for the Pedestal and Edge Physics ITPA Topical Group 2006 *Plasma Phys. Control. Fusion* **48** A149

[31] Sauter O., Angioni C. and Lin-Liu Y.R. 1999 *Phys. Plasmas* **6** 2834

[32] Koh S., Chang C.S., Ku S., Menard J.E., Weitzner H. and Choe W. 2012 *Phys. Plasmas* **19** 072505

[33] Callen J.D., Cole A.J., Hegna C.C., Mordijck S. and Moyer R.A. 2012 *Nucl. Fusion* **52** 114005

[34] Ishizawa A. and Nakajima N. 2007 *Nucl. Fusion* **47** 1540